Available online at www.sciencedirect.com
SCIENCE DIRECT®
PERGAMON
Electrochimica Acta 48 (2003) 1675–1684
ELECTROCHIMICA Acta
www.elsevier.com/locate/electacta

Application of a.c. impedance technique to the study of the proton diffusion process in the porous MnO_2 electrode

Deyang Qu *

Emtech, 2486 Dunwin Dr., Mississauga, Ont., Canada

Received 11 October 2002; received in revised form 15 January 2003

Abstract

The proton diffusion coefficient in γ-MnO_2 at various stages of discharge of an electrolytic manganese dioxide electrode has been determined taking into consideration the true molar volume and the electrochemically accessible surface area of MnO_2. The unique electrochemical cell which allows the electrode expansion during the discharge to be monitored in situ was reported. The a.c. impedance technique and the transmission line equivalent circuit were used. Electrode ohmic resistance, Faradaic resistance, and double-layer capacitance were also obtained by means of numerical fitting of the impedance data using the transmission line model.

Keywords: MnO_2; EMD; Proton diffusion coefficient; a.c. impedance; Transmission line model

1. Introduction

MnO_2 is one of the most widely used material for many battery systems, e.g. primary and secondary alkaline manganese dioxide/zinc cells and primary/secondary Li or Li ion cells. The cathodic and anodic mechanisms of the operation of several kinds of MnO_2 have been extensively studied by various methods and techniques. For the discharge of γ-MnO_2 in alkaline electrolyte, Kozawa and coworkers [1–4] postulated a two-step mechanism for the reaction. The first step involves homogenous proton diffusion in the lattice of γ-MnO_2, while the second step is a heterogeneous process involving soluble Mn^{3+} species [5]. In most applications, except for those at very low discharge current density, γ-MnO_2 is rarely discharged to the heterogeneous step.

The proton diffusion step of the reduction is the key process during the first discharge step of manganese dioxide. The significance of the proton diffusion was first reported by Coleman [6] in 1946 and yet the value of the proton diffusion coefficient in manganese dioxide is still not well known. There are few electrochemical techniques developed to measure the diffusion coefficient in the solid-state electrodes, e.g. current pulse relaxation [7], a.c. impedance spectroscopy [8], potential step chronoamperometry [9], and galvanostatic intermittent titration [10]. The application of those methods to determine the Li ion diffusion coefficient in the solid phase has been reviewed [11]. The proton diffusion within electrolytic manganese dioxide (EMD) has also been investigated by various electrochemical techniques [12–14]. Atlung and Jacobsen [8] applied a.c. impedance spectroscopy to determine the proton diffusion coefficient of EMD in a potassium chloride/potassium hydroxide solution. By assuming that the electrochemical accessible surface area was the same as BET surface area, the diffusion coefficient was determined to be 2.6×10^{-16} cm^2 s^{-1}. Taking into consideration the EMD crystal structure, Zheng and Xia [15] proposed a "double-plane" diffusion model, which described the proton diffusion within MnO_2 lattice occurring in both directions along the *C*-crystallographic axis through $[1 \times 2]$ channel. Most recently, by means of the potential step technique, Chabre and Pannetier [16] measured the proton diffusion coefficient of EMD at various stages of discharge. Even though the authors questioned the results of diffusion coefficient obtained, since the electrochemical active surface area of the electrode can

* Present address: Rayovac, 601 Rayovac Dr., Madison, WI 53719, USA. Tel.: +1-608-275-4745; fax: +1-608-275-4992.
E-mail address: qu@rayovac.com (D. Qu).

0013-4686/03/$ - see front matter
doi:10.1016/S0013-4686(03)00146-4

change during the discharge process, they still believed that the BET surface area provided the best estimate.

To avoid estimating the true surface area (A) of porous MnO_2 electrode, $A\sqrt{D}$ was considered as a battery activity parameter [17] to gauge the ionic and proton diffusions of EMD electrode. The two functions clearly represent two different structural/dynamic aspects of manganese dioxide. A stands for the porosity that determines the transport of water and hydroxide ions throughout the matrix of the porous electrode from the bulk solution to the surface of individual solid particle [23]. D stands for the proton diffusion coefficient inside MnO_2 lattice. D is determined by the structure of MnO_2 itself. Reasonable estimation of true surface area (A) of the electrode is the key to obtain the proton diffusion coefficient (D).

2. Experimental

2.1. Material

EMD was obtained from KerrMcGee Corporation. KS6 synthetic graphite was from Lonza (now Timcal). Teflon suspension (T-30) used was from Dupont.

2.2. Electrolyte, and reference- and counterelectrodes

An amount of 30 wt.% aqueous potassium hydroxide solution was used as the electrolyte in all experiments at 298 ± 1 K. All potentials reported were referred to Hg/HgO reference electrode immersed in KOH of the same concentration as the experimental electrolyte. A Ni mesh counterelectrode was used.

2.3. Construction of the electrodes used in the experiments

EMD was mixed thoroughly with Lonza graphite (KS6) at 9:1 (EMD:graphite) weight ratio using high-speed electric grinder for 10 min. 0.5 wt.% (dry material) of a Teflon suspension (Dupont T-30) was then added into the black mix as binder. The resulting mix was air-dried. Two grams of the material was pressed at a pressure of 9 t to form the electrode. The diameter of the electrode was 22.0 ± 0.2 mm and the thickness of the electrode was 1.8 ± 0.2 mm. The electrode was then mounted in the electrochemical cell as shown in Fig. 1. Before the electrochemical measurements were performed, all electrodes were vacuum-wetted to ensure the electrolyte penetration into the pores. The electrode was discharged by constant current at either 61.6 mA g^{-1} (C/5) or 30.8 mA g^{-1} (C/10) rates.

2.4. Experimental techniques and instrumental details

The a.c. impedance measurements were conducted by means of a Solartron Electrochemical Interface 1278 and Solartron FRA 1255 controlled by ZPLOT. The equivalent circuit fitting of the a.c. impedance data was done using ZVIEW. Both ZPLOT and ZVIEW were the electrochemical software from Scribner. Constant current discharge was carried out by means of HOKUTO Denko HA 301 potentiostat/galvanostat controlled by Q&R Smart Data package. A Micromeritics ASAP 2000 porosity meter was used for the measurement of surface area. The displacement sensor was purchased from TRANS-TEK and the data were also collected by the Q&R Smart Data package. Since the experiment to determine the slope of the open-circuit voltage (OCV) versus the mole fraction of MnO_2 ($\partial V_{ocv}/\partial x$) took very long time, in order to prevent the reduced MnO_2 becoming reoxidized by dissolved oxygen, the cell was vacuumed and backfilled with N_2 in an airtight chamber and the experiment was done under N_2 atmosphere.

2.5. Electrochemical cell

The electrochemical cell used in the experiments is shown in Fig. 1. The left compartment (8) was used to accommodate EMD working electrode (2). The electrode was mounted between two perforated Ni disks (3). The Ni block (4) was served as a spacer. Both the perforated disks (3) and the Ni spacer (4) were tightly fitted against the cell wall for two reasons; first, to prevent horizontal movement during the electrode expansion, thus improving the accuracy of the measurement; second, to limit the air diffusion into the MnO_2 electrode, thus minimizing the reoxidation of the reduced Mn by oxygen and also preventing carbonate formation on the electrode during the course of discharge. Part (6), which sat on the top of the spacer, transformed the electrode height change during the discharge. The pressure on the electrode was kept constant by keeping the same spring (7) force. The vertical hole (5), which was linked to the working electrode compartment by a horizontal capillary, was used to accommodate Hg/HgO reference electrode. The right compartment (10) housed Ni counterelectrode (9). The two cell houses were connected by the electrolyte bridge (12) and the whole cell was mounted on the solid base (11). The cell was made of Teflon to resist the strong alkaline electrolyte. The top part was the fixture of the displacement sensor (1), and the metal probe of the sensor sat on the top of part (6). The MnO_2 electrode fitted tightly into the cell compartment and there was little room for the electrode to expand in the horizontal direction. The expansion of the disc electrode in the perpendicular direction was measured by the displacement transducer operating on the induction principle.

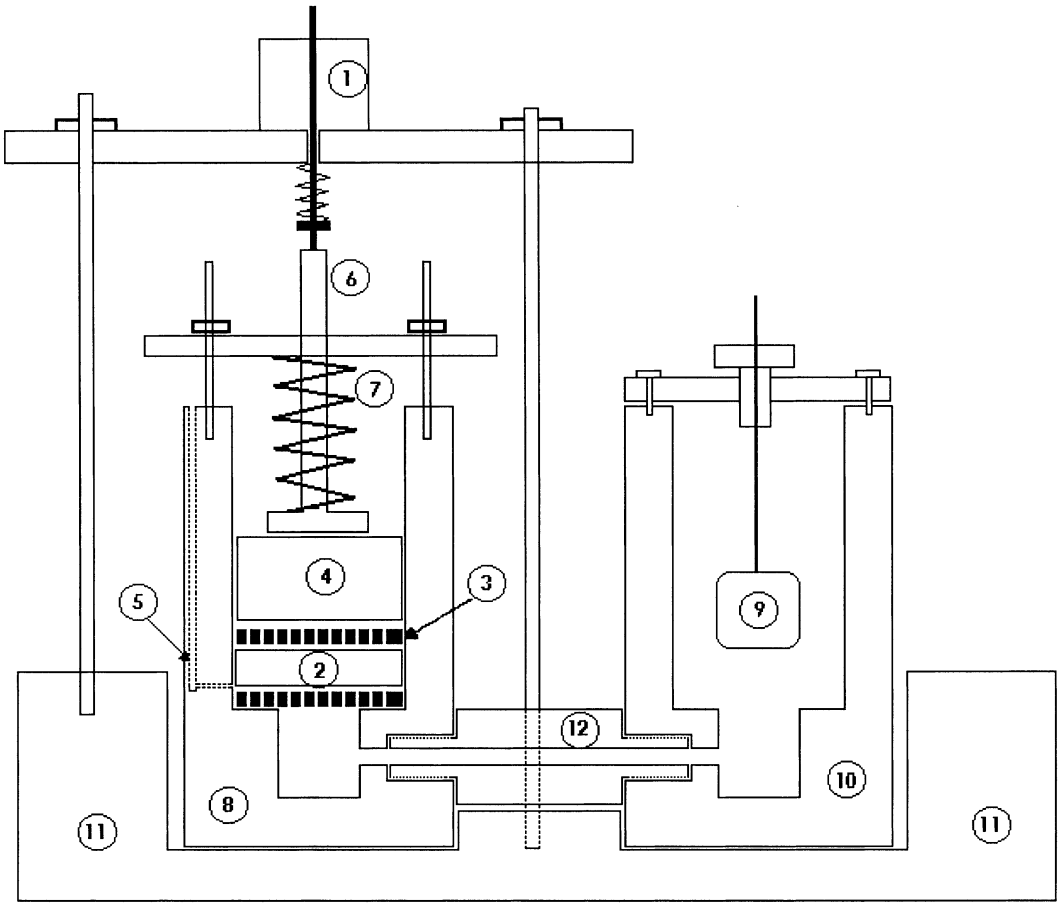

Fig. 1. Electrochemical cell used in the experiments: 1, displacement transducer; 2, EMD working electrode; 3, perforated Ni disk; 4, Ni spacer; 5, hole for reference electrode; 6, Ni rod to transform electrode height change; 7, calibrated spring; 8, Teflon working electrode compartment; 9, Ni counterelectrode; 10, Teflon counterelectrode compartment; 11, plastic base.

The electrode expansion during the discharge was monitored by the sensor and recorded as a voltage signal by means of the data acquisition software.

3. Results and discussion

3.1. Theory and equivalent circuits

A porous electrode has a pore distribution resulting from the particle size distribution of the material involved and the electrode fabrication process. Pores with different size distributions have different time constants, and the ionic diffusion rate inside the pores of different sizes varies. Also, problems of different kind arise due to finite resistance of the particles and the supporting electrolyte, and to interparticle contact resistance. All these situations can be represented by an infinite transmission line model [18]. A porous electrode that involves Faraday charge transfer can be represented as a transmission line equivalent circuit shown in Fig. 2A [19,20]. Two types of currents through the interface of the electrode should be distinguished. They are the current due to the proton insertion and the electron migration inside EMD particles (I_f), and the non-Faraday current to charge/discharge the double layer. The Faraday branch may be represented by a charge transfer resistance R_{ct} and by Warburg impedance Z_w, while the non-Faraday displacement current branch may be represented by the distributed double-layer capacitors, C_{dl}. The distributed capacitance and resistance are used to represent energy dissipation in a porous electrode.

Fig. 2A represents the porous electrode matrix for the ionic diffusion with the local proton intercalation into the lattice of EMD. The mathematical equation of *RC* transmission line has the same form as the diffusion equation since the process taking place in *RC* circuit may be treated as electronic diffusion into a semi-infinite medium. So the transmission line equivalent circuit in Fig. 2A can be simplified as in Fig. 2B. CPE is a constant-phase element and its impedance can be represented as [21]

$$Z = \sigma'\omega[\cos(\tfrac{1}{2}m\pi) - \mathrm{i}\,\sin(\tfrac{1}{2}m\pi)] \quad (1)$$

where σ' is termed as the CPE factor and m the CPE

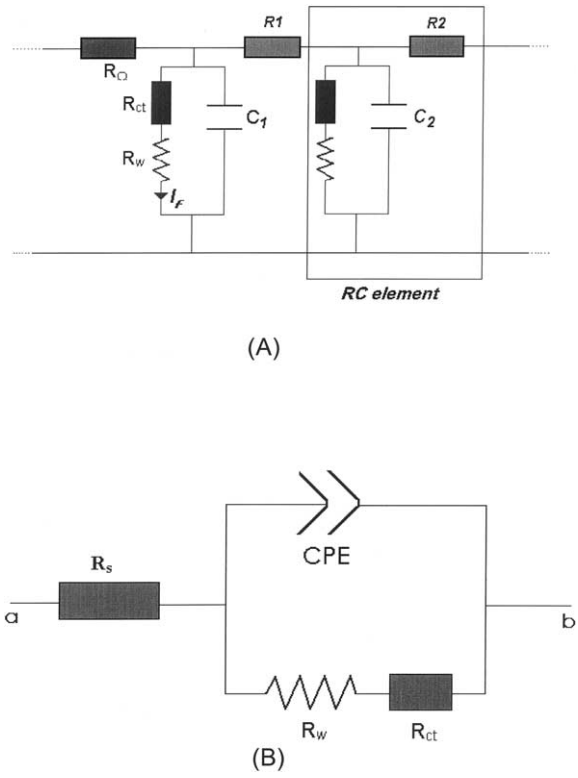

Fig. 2. Transmission line equivalent circuit model used in the a.c. impedance fitting. R_s or R_Ω, ohmic resistance; R_{ct}, Faradaic resistance; C, distributed double-layer capacitance; R, distributed resistance; R_w, Warburg resistance; CPE, constant-phase element.

exponent. When $m = 1/2$, Eq. (1) stands for Warburg impedance of semi-infinite diffusion ($\omega \gg D/l^2$, where l is the diffusion length) and it can be written as

$$Z = \sigma(1 - \mathrm{i})\omega^{-1/2} \tag{2}$$

where

$$\sigma = \frac{V_m}{nFA(2D)^{1/2}} \frac{\partial V_{ocv}}{\partial x} \tag{3}$$

then

$$D = \frac{1}{2}\left[\frac{V_m}{nFA\sigma} \frac{\partial V_{ocv}}{\partial x}\right]^2 \tag{4}$$

where D is the proton diffusion coefficient in EMD lattice, $\partial V_{ocv}/\partial x$ the slope of the open-circuit voltage V_{ocv} versus the mole fraction of MnO_2, and V_m the molar volume of MnO_2. R_{ct} in Fig. 2 is the charge transfer resistance of MnO_2.

A Warburg impedance occurs when charge carriers diffuse through a material. Lower frequencies correspond to the diffusion deeper into the material. If the material is thin, low frequencies will penetrate the entire thickness and the impedance would be a finite Warburg impedance which can be expressed as [22]

$$Z = (1 - \mathrm{i})\sigma\omega^{-1/2} \tanh\left\{\delta\left(\frac{\mathrm{i}}{\omega D}\right)^{1/2}\right\} \tag{5}$$

where δ represents the effective diffusion thickness and D the effective diffusion coefficient of the particle. If the material is thick enough, so that the lowest frequency applied does not fully penetrate the layer, it must be interpreted as semi-infinite Warburg impedance. In the case of EMD electrode, the crystal size of MnO_2 in EMD was about 28.6 Å calculated from 22° 2θ X-ray diffraction peak, which corresponds to the (1 1 0) plane of the orthorhombic lattice of γ-MnO_2 by Scherrer equation. It is worth emphasizing that even though calculating the crystal size of EMD by Scherrer equation from (1 1 0) X-ray diffraction peak is the common practice among EMD and alkaline battery manufactures [23], one should realize that EMD is the intergrowth of ramsdellite domains and pyrolusite domains according to De Wolff model. The width of (1 1 0) peak is influenced by both the crystal size and the defects. Assuming that the diffusion length for the protons is equivalent to the crystal size of MnO_2 and the proton diffusion coefficient is in the range 10^{-15}–10^{-18} cm^2 s^{-1}, as reported in the literature, then D/l^2 would be in the range 0.01–10^{-5} Hz. Moreover, EMD is well known as a highly disordered material; the proton diffusion at the practically useful potential (>0.45 versus Hg/HgO) only involves the $[1 \times 2]$ channel in the ramsdellite domains of the solid solution. So, the actual length of the proton diffusion would be the size of the ramsdellite unit. Either De Wolff disorder or microtwinning, or other kinds of stresses can interrupt the homogeneity of ramsdellite unit and thus put obstacles on the proton diffusion pathway. So the diffusion length for the protons would be much shorter than the size of the crystal. The condition for semi-infinite diffusion may not be met in the case of the

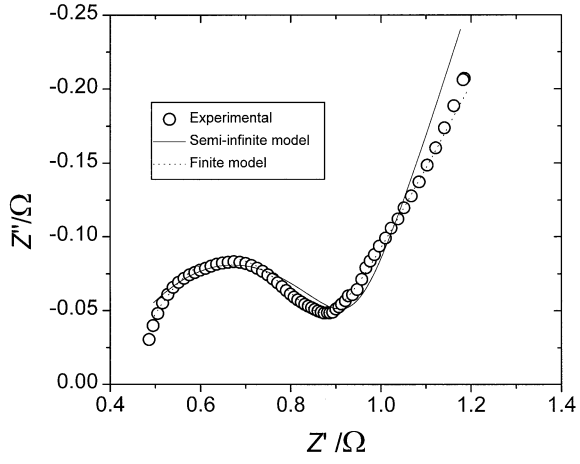

Fig. 3. a.c. impedance response for a non-discharged EMD electrode. Numerical fittings were based on semi-infinite model (solid line) and finite model (dashed line).

proton diffusion inside EMD. Fig. 3 shows the complex plane plot for EMD electrode before discharge and the fitting of results based on the semi-infinite diffusion model and the finite diffusion model, respectively. The finite diffusion model seems to fit the experimental data better, especially in the low-frequency range. However, for the sake of the comparison with the results reported in the literature, in which a semi-infinite diffusion model was almost exclusively used, the results reported in this paper are based on the semi-infinite diffusion model. The application of the finite diffusion model will be reported in a later publication. Table 1 tabulates the fitting results for both models.

3.2. Ionic diffusion inside the porous electrode

A porous MnO_2 electrode consists of an electronically conductive solid medium with a high surface area and electrolyte or air-filled pores. Further charge transport processes in the MnO_2 cathode comprise the ionic diffusion inside the matrix of the porous electrode, through pores of various sizes, and the proton diffusion throughout the lattice of MnO_2. The latter is the process being investigated in this paper.

Most electrochemical investigations of the manganese dioxide electrode ignored the impact of the electrode porosity assuming that the influence can be minimized by the use of low EMD to graphite ratio, flooded electrolyte, and thin electrode [24]. This approach, however, is not valid for the commercial EMD cathodes in primary and secondary alkaline MnO_2/Zn cells. Since all the cathodes in those cells are in bobbin design with a high EMD to graphite ratio and are starved for electrolyte in order to ensure high energy density. A good example to demonstrate the impact of porosity is the approximately inverse correlation between surface area of EMD and their discharge capacity in alkaline electrolyte [23]. A real porous electrode consists of the pores with various sizes, the pores can be either non-interconnected or interconnected into a network matrix. Obviously, there will be no single value for the ionic diffusion coefficient in the porous electrode, since the ionic diffusion rate in the pores with different sizes varies. So, the mean ionic diffusion coefficient in the porous electrode is highly dependent on the modulation frequency. Euler [25] suggested that the influence of the pores is limited to the low-frequency part of impedance and consequently the reaction for the manganese dioxide can be estimated from high-frequency range. An attempt in this direction was undertaken by Qu [20] by means of a.c. impedance measurements on the MnO_2 cathode of several commercial LR6 cells. A modified transmission line equivalent circuit was used to simulate the MnO_2 porous electrodes. In the general transmission line model [19], the diffusion can be represented by the distributed elements, which relate to the energy dissipation among the pores of various sizes. Its impedance is represented by CPE as shown in Fig. 2B. The proton diffusion inside manganese dioxide lattice, however, can be simulated by Warburg impedance in Fig. 2B.

Under the experimental condition described in Section 2.3, the process of proton diffusion in the lattice of EMD is considerably slower than the ionic diffusion in the electrolyte solution, since 30 wt.% KOH electrolyte was used to largely overcome the ionic resistance and pH polarization, which allowed the solution-based processes in the cathode to accelerate to the point that the solid-state proton diffusion became the rate-determining step. In addition, the electrode was vacuum-wetted to ensure that most of the pores were fully filled with the electrolyte and the a.c. impedance measurements were not taken until the electrode came to equilibrium.

Table 1
Fitting results for non-discharged EMD electrode based on equivalent circuit shown in Fig. 2

Parameters	Semi-infinite	Finite
Ohmic resistance, R_s (ohm)	0.367	0.378
Charge transfer resistance, R_{ct}	0.601	0.510
CPR factor, σ'	7.025	12.61
CPE exponent, m	0.334	0.40
Double-layer capacitance (at 0.0001 Hz) (F)	28.5	3.5
Warburg factor, σ	0.061	
∂^2/D (s)		82.7

3.3. MnO_2 lattice expansion and the change of the MnO_2 molar volume during discharge

It is well known that the MnO_2 electrode expands during discharge [26]. Fig. 4A and B show the discharge curves for EMD electrodes and the corresponding electrode expansion curves, respectively. The MnO_2 electrodes were discharged at two different rates: 30.8 mA g^{-1} (C/10) and 61.6 mA g^{-1} (C/5). Fig. 4A shows from the results of three tests per discharge rate that the reproducibility of the discharge tests was very high. Fig. 4B shows the perpendicular expansion of the MnO_2 electrode at various depths of discharge. The results of three tests for each discharge rate are plotted in Fig. 4B. Good reproducibility was demonstrated again.

Vertical expansion of the electrodes was plotted against the depth of discharge (DOD) in Fig. 4B. It is clear that the degree of expansion for EMD electrode is a function of DOD or the oxidation states of MnO_2 and was not influenced by the discharge rate. Apparently, three regions can be distinguished in the electrode expansion curves as shown in Fig. 4B. In region I, which covered up to 10% of DOD, there was little expansion for the electrodes at both discharge rates. The expansion for the MnO_2 electrode results from the

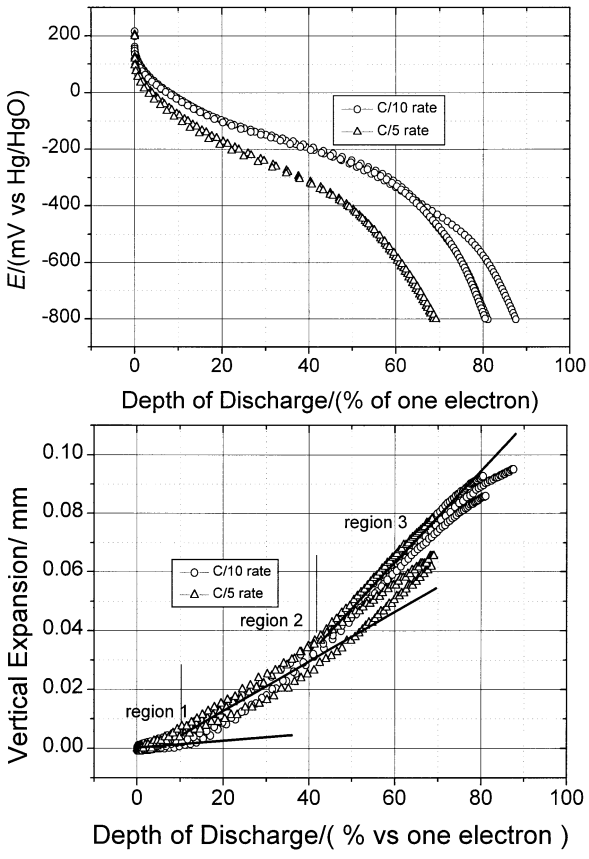

Fig. 4. Discharge curves for EMD electrodes (A) at 61.6 and 30.8 mA g^{-1} current density and the corresponding electrode expansion curves (B).

insertion of the protons and the change of ionic radii of Mn species in the MnO_2 lattice during discharge. Table 2 tabulates the ionic radii of the ions in MnO_2 lattice [27]. The size of Mn species increases significantly from their 4+ oxidation state to 3+ oxidation state causing the lattice expansion of MnO_2. The expansion of the particles would lead to a shifting of the particle to particle contact points and reformation of the established porous electrode matrix. Since the MnO_2 electrode was highly porous with the pores occupied by either air or electrolyte, the expansion of particle size may initially be accommodated by reducing the porosity of the electrode. Thus, even with the expansion of EMD particles, the apparent volume of the electrode hardly changed for the initial 10% of discharge. In region II, the

Table 2
Ionic radii in MnO_2 lattice

Ions	Radius (Å)
O^{2-}	1.40
OH^-	1.37
Mn^{4+}	0.53
Mn^{3+}	0.645
Mn^{2+}	0.833

expansion of the MnO_2 electrodes has a linear relationship with DOD. The expansion, obviously, resulted from the MnO_2 lattice expansion during discharge. Although the electrodes expanded linearly during the discharge in region III as shown in Fig. 4B, the slope of the expansion curves for region III changed significantly. The change took place at about 45% of the one-electron capacity of MnO_2. The electrode expansion in region III still resulted from the MnO_2 lattice expansion, but the slope change at 45% DOD was believed to result from Jahn-Teller deformation which changes the symmetry of MnO_2 structure.

Although the degree of the expansion for MnO_2 lattice is only related to DOD and not to the discharge rate as mentioned earlier, the crystal structure of EMD and the physical structure of MnO_2 electrode have been proved to have impacts on the electrode expansion. The influence will be reported elsewhere. Assuming that the volume of the graphite did not change during the course of discharge, Fig. 5 shows the change of MnO_2 molar volume due to the lattice expansion during discharge.

3.4. Real accessible surface area of the MnO_2 electrode during discharge

The surface area of a given mass of solid powder material is closely related to the size of the constituent particles. Those powder particles stick together and pores are formed in those aggregated particles. Pore size and pore size distribution depend on the size and shape of the powder particles and how they are packed together. The total surface area of a porous electrode is the sum of the surface area contributed from all the pores. The pores with different sizes have different time constants and the surface area associating to the pores with various sizes has different accessibility. The kinetic of accessibility of the pores with various sizes in the porous electrodes has been investigated in great detail by Qu [18,20].

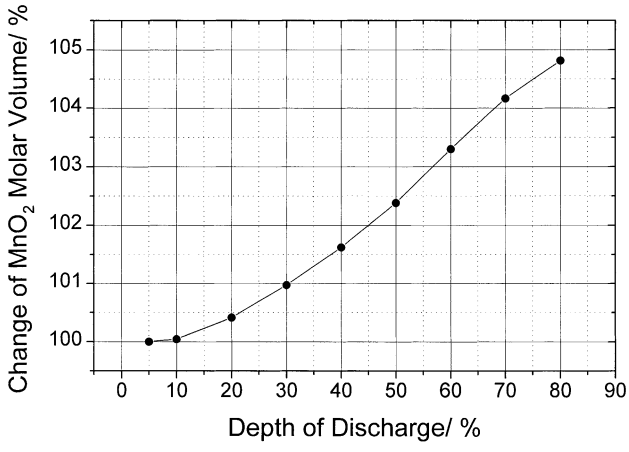

Fig. 5. MnO_2 molar volume change at various stages of discharge.

The surface area of the manganese dioxide electrode, which is electrochemically accessible at certain stage of discharge, is a very important parameter for the performance of the electrode. The higher the accessible surface of the electrode, the lower the current density and hence the smaller the overpotential. To determine the proton diffusion coefficient by means of Eq. (4), the electrochemical active surface area (A) is needed. Traditionally, there are three ways to deal with A in the equation:

1) Set A as a unit.
2) Set A as BET surface area of the electrode.
3) Set A as the geometric surface area of the electrode.

Approach 1 fails to take into consideration the real surface area of EMD. It is well known that the proton diffusion coefficient is mainly dictated by the crystal structure of EMD, which is determined by the electrolysis conditions, e.g. plating current density and plating bath temperature. The variation of the electrolysis conditions, however, can significantly change the surface area of EMD. So, the proton diffusion coefficient inside EMD would not be determined accurately without taking the real surface area into consideration. Both the approaches 1 and 2 assume that the active surface area of the electrode does not change during the course of discharge. As mentioned previously, the electrode expansion may change the porosity of the porous electrode during discharge, and the assumption that the active surface area does not change during the course of discharge may not be valid. Approach 3 may be only valid for a thin-layer electrode, e.g. single layer of MnO_2 deposited on either Au or Pt electrodes.

In-depth studies were conducted by Soffer and coworkers [28–30] in the accessibility of micropores to aqueous solution. It has been concluded that since the size of single N_2 molecule is similar to that of OH^- and K^+ ions or water molecule in aqueous solution, those micropores that can accommodate adsorbed nitrogen molecule at 77 K are also available for the electroadsorption of simple hydrated ions or water molecule at low, concentration-dependent rate. Thus, in the case of porous EMD electrode, the initial electrochemically accessible surface area can be treated as the same as the BET surface area of the electrode. In our case, the initial accessible surface area was the true EMD surface area in the electrode; the surface area of graphite was excluded since it did not contribute to the diffusion coefficient calculation. The BET surface area of EMD was 45.3 $m^2\ g^{-1}$.

The capacitance stored in the double layer of a porous electrode is proportional to the surface area of the electrode and inversely proportional to the thickness of the double layer. Since strong KOH solution was used in EMD electrode, the double-layer capacitance of the electrode can be treated as proportional to the surface area with the establishment of a double layer. The surface area must be electrochemically accessible [20]. Assuming that the specific capacitance (mF cm^{-2}) did not change significantly throughout discharge, the change of the accessible surface area can be experimentally determined by measuring the change of the double-layer capacitance during the course of discharge. The assumption that the specific double-layer capacitance of EMD remained unchanged during the course of the discharge is valid based on the fact that the double-layer capacitance is a surface phenomenon; the initial reduction of MnO_2 is a three-dimensional homogeneous reaction with proton diffusion into the lattice of MnO_2, and the surface modification is minimum. The significant surface change only starts at the later stage of discharge when the MnO_2 structure collapses and the Mn^{3+} species start to dissolve. The role of dissolution of Mn(III) species was investigated in great deal by Qu et al. [31]; the Mn(III) species do not start to dissolve significantly till 70% of DOD, which coincides with the end of the sloping discharge curve. The sloping profile of the discharge curve was the evidence of single-phase homogeneous reaction. The initial double-layer capacitance of the electrode is listed in Table 1. Fig. 6 shows the change of real surface area of MnO_2 electrode at various DODs. The accessible surface area decreased about 60% during the initial 20% DOD. The decrease of the surface area during the discharge was believed to result from the expansion of the MnO_2 particles. As the volume of the cathode changes, some pores, especially those with small opening, could be sealed, thus the surface area being reduced. It is worth emphasizing that the rapid change of accessible surface area at the early stage of discharge is a common phenomenon for alkaline MnO_2 cathode. As mentioned previously, the initial expansion of MnO_2 particles was almost exclusively used to modify the porosity of the electrode. The change primarily depends on the cathode fabrication process and the choice of cathode ingredients. The accessible surface area can increase or decrease as demonstrated in

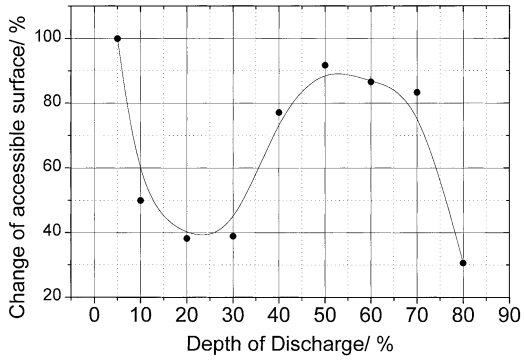

Fig. 6. The change of the accessible surface area for EMD electrode at various depths of discharge.

the early publication [20]. During the range 20–50% DOD, the real surface area started to increase and recovered to almost 90% of its initial surface area. The surface area increase in the mid-discharge is also believed to be the result of the expansion of the MnO_2 particles. As the particle size of MnO_2 increased, the geometric surface area would increase together with the electrode volume. Also, changing of the particle size would result in morphology modification, which could create new pores. Up to 50% DOD, the conclusion from Fig. 6 is consistent with that from Fig. 4B. The sudden decrease of the accessible surface area in the later discharge of the electrode is difficult to understand. Jahn-Teller deformation cannot explain the phenomenon. It might be due to the significant change of specific capacitance (mF cm^{-2}) for the electrode, since γ-MnO_2 structure could collapse at the later stage of discharge and the surface characteristics of MnO_2 could change significantly.

3.5. Proton diffusion coefficient in EMD

The proton diffusion coefficient in the lattice of MnO_2 can be calculated using Eq. (4). As described in the previous two sections, the molar volume of MnO_2 (V_m) at various stages of discharge and the real surface area (A) at various stages of discharge can be obtained experimentally through the measurements of the electrode expansion and the change of the double-layer capacitance during discharge, respectively. σ can be obtained by the numerical fitting for the a.c. impedance results taken at various stages of discharge. Fig. 7 shows the change in OCV versus DOD and its differential curve. With all the necessary information, the proton diffusion coefficient at various stages of discharge can be calculated using Eq. (4). Fig. 8 shows the proton diffusion coefficient at various DODs. The values of the proton diffusion coefficient inside the lattice of EMD have been shown to be 10^{-15}–10^{-16} $cm^2\ s^{-1}$ depending on DOD.

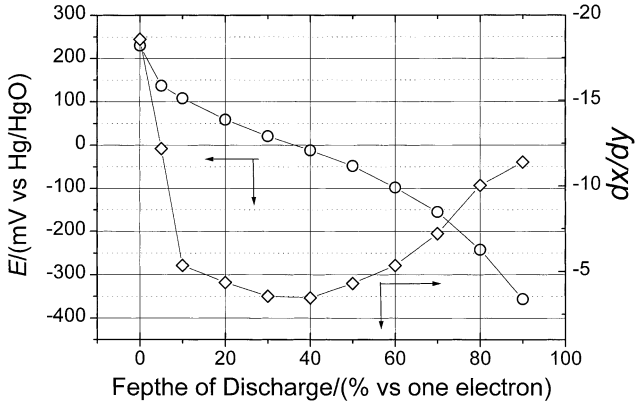

Fig. 7. OCV versus DOD curve and dy/dx curve for the MnO_2 electrode at various depths of discharge.

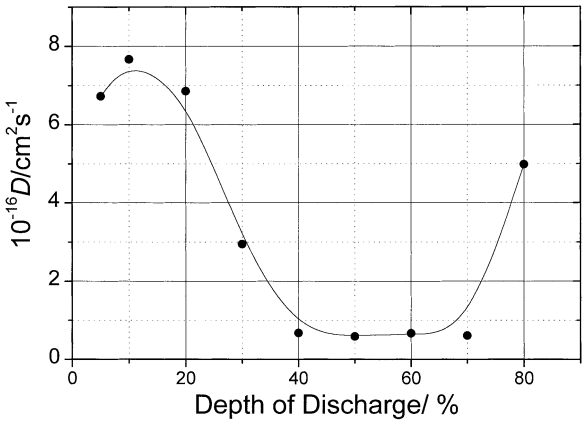

Fig. 8. Proton diffusion coefficients inside MnO_2 at various depths of discharge.

The proton diffusion coefficient inside MnO_2 lattice is closely associated with the crystal structure, especially with crystal defects of EMD. Detailed structure analysis for the material is necessary to explain the change of the coefficient during discharge. Although the detailed investigation of the structural impact on the proton diffusion will be reported elsewhere, a few quick observations can be made in Fig. 8. It is believed that during the discharge range of one electron, the majority of protons were intercalated into the [1 × 2] channel of the ramsdellite domain of the compounds. The intercalated proton can be located either on the pyramidal or the planar oxygen sites, which obviously have slightly different energy with respect to each other. The localized Jahn-Teller distortion, which happened at about 45–50% of DOD, did not seem to have much impact on the proton diffusion. Jahn-Teller distortion may not have significant impact on diffusion until it extends over the whole lattice of MnO_2, which is believed to result in a sudden increase of the proton diffusion coefficient in the very end of discharge. In addition, the proton diffusion rate is also related to the ability of the crystal lattices to undergo expansion, as Mn^{4+} ions are being replaced by Mn^{3+} ions. The proton diffusion rate depends thus on the ability of the structure to accept electrons. Practically, the surface area and structural water are important parameters.

3.6. Charge transfer resistance, R_{ct}

The mechanism for MnO_2 reduction starts from the physical adsorption of H_2O molecules on the surface of MnO_2 particles. The protons from the absorbed water molecules then intercalated into the lattice of MnO_2 after the cleavage of O–H bonds. Three major steps with different energy barriers are as follows:

1) H_2O molecule absorption.
2) O–H bond breakage.

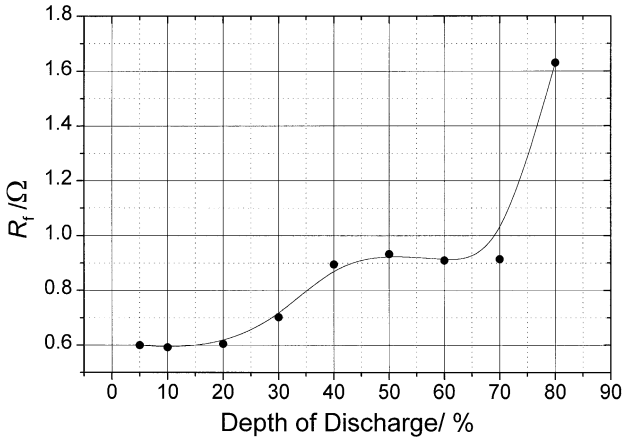

Fig. 9. Change of Faradaic resistance of MnO_2 electrode at various depths of discharge.

3) H crossing EMD surface into the bulk of crystal lattice.

R_{ct} in Fig. 2 can be represented as

$$R_{ct} = \frac{RT}{mFi_0} \tag{6}$$

where i_0 is the exchange current which can be represented as

$$i_0 = \frac{1}{V_m}\{nFAk^0C^{1/2}[x(1-x)]^{1/2}\} \tag{7}$$

then

$$R_{ct} = \frac{RTV_m}{n^2F^2Ak^0C^{1/2}}[x(1-x)]^{-1/2} \tag{8}$$

where C is the surface concentration of H_2O molecules for steps 1 and 2, and concentration for protons for step 3 at the interface of the MnO_2 particles, and k^0 the standard rate constant for the each surface proton generation steps, and thus R_{ct} is believed to relate not only to the surface condition of EMD particles, but also to the water activity in the vicinity of EMD particles. High R_{ct} will result in high electrochemical overpotential during discharge. R_{ct} can be used to evaluate the quality of EMD. The R_{ct} value can change significantly among different EMD. Fig. 9 shows the change of R_{ct} of the EMD electrode at various stages of discharge. The gradual increase of R_{ct} starting at about 25% DOD may result from the localized Jahn-Teller distortion, especially those close to the surface of EMD crystal and the change of H_2O activity at the MnO_2 interface.

4. Conclusions

The proton diffusion process in EMD electrode has been investigated by means of a.c. impedance and numerical fitting techniques. The proton diffusion coefficients at various stages of discharge have been measured by taking into consideration the true molar volume of MnO_2 and the real surface area of the electrode. The following points are of value to be noted:

1) Determination of proton diffusion coefficient inside the lattice of EMD is the essential step to the understanding of the proton intercalation process.
2) Together with other techniques, a.c. impedance is believed to be an excellent method for the determination of the diffusion coefficient for the solid-state intercalation process.
3) The true molar volume of MnO_2 at various stages of discharge can be obtained experimentally by carefully measuring the electrode expansion during discharge.
4) It is believed that nitrogen absorption BET surface area of the electrode can be treated as the real surface area of the electrode.
5) The electrochemically accessible surface area of EMD electrode during discharge can be obtained through the determination of the change of the double-layer capacitance at various stages of discharge.
6) Localized Jahn-Teller deformation happens in the middle stage of discharge and plays a very important role in the discharge of EMD.
7) The techniques used in the study of the proton diffusion in EMD are also valid to be used to investigate other systems involving particle diffuison in the solid-state material, e.g. Li diffusion in $LiMn_2O_4$ or $LiCoO_2$.

References

[1] A. Kozawa, J.F. Yeager, J. Electrochem. Soc. 115 (1968) 1003.
[2] A. Kozawa, R.A. Powers, J. Electrochem. Soc. 113 (1966) 870.
[3] A. Kozawa, R.A. Powers, Electrochem. Tech. 5 (1967) 535.
[4] A. Kozawa, R.A. Powers, J. Electrochem. Soc. 115 (1960) 112.
[5] D.Y. Qu, L. Bai, C.G. Castledine, B.E. Conway, W.A. Adams, J. Electroanal. Chem. 365 (1994) 247.
[6] J.J. Coleman, Trans. Electrochem. Soc. 90 (1946) 545.
[7] R.B. Hodjean, J. Farcy, et al., J. Electrochem. Soc. 143 (1996) 2083.
[8] S. Atlung, T. Jacobsen, Electrochim. Acta 21 (1976) 575.
[9] K. Kamamura, K. Yuasa, Z. Takehara, J. Power Sources 20 (1987) 127.
[10] T. Uchina, Y. Marihaua, H. Ikuta, et al., J. Electrochem. Soc. 43 (1996) 2606.
[11] X. Wang, Q. Zhou, Y. Zhang, Chin. J. Power Sources 23 (1999) 335.
[12] A.B. Scott, J. Electrochem. Soc. 107 (1960) 941.
[13] F. Kornfeil, J. Electrochem. Soc. 109 (1962) 349.
[14] J.P. Gabano, J. Seguret, J.F. Laurent, J. Electrochem. Soc. 117 (1970) 147.
[15] H. Zheng, X. Xia, J. Electrochem. Soc. 136 (1989) 2771.
[16] Y. Chabre, J. Pannetier, Prog. Solid State Chem. 23 (1995) 1.

[17] P. Brouillet, A. Grund, F. Jolas, R. Mellet, C. R. Acad. 257 (1963) 3390.
[18] D.Y. Qu, H. Shi, J. Power Sources 74 (1998) 99.
[19] R. De Levie, Electrochim. Acta 8 (1963) 751.
[20] D.Y. Qu, J. Power Sources 102 (2001) 270.
[21] C. Ho, I.D. Rastrick, R.A. Hugins, J. Electrochem. Soc. 127 (1980) 343.
[22] J.L. Dawson, D.G. John, J. Electroanal. Chem. 110 (1980) 37.
[23] T.N. Andersen, J.M. Derby, Electrochemistry in Transition, Plenum Press, New York, 1992, pp. 655–678.
[24] A. Kozawa, R.A. Power, J. Electrochem. Soc. 106 (1959) 745.
[25] J. Euler, Electrochim. Acta 4 (1961) 27.
[26] R. Chemelli, J. Gsellmann, G. Korber, K. Kordesch, IBA Manganese Dioxide Symposium (Tokyo) 2 (1980) 150.
[27] P. Ruetschi, J. Electrochem. Soc. 131 (1984) 2737.
[28] A. Soffer, M. Folman, J. Electroanal. Chem. 25 (1972) 38.
[29] J. Koresh, A. Soffer, J. Electrochem. Soc. 124 (1977) 711.
[30] J. Koresh, A. Soffer, J. Electroanal. Chem. 147 (1983) 223.
[31] D.Y. Qu, B.E. Conway, L. Bai, Y.H. Zhou, W.A. Adams, J. Appl. Electrochem. 23 (1993) 693.